Cosmic Collision: Insights from Magnetohydrodynamic Simulations of a Colliding Neutron Star and White Dwarf

Ishan F. Ghosh-Coutinho [ID],[1] Xander Dewulf [ID],[1] and Yian Xia [ID][1]

[1]*Institute of Astronomy, KU Leuven, Celestijnenlaan 200D, 3001, Leuven, Belgium*

ABSTRACT

Neutron Stars (NS) and White Dwarf (WD) systems (NS-WD or WD-NS) can lead to mergers or collisions resulting in luminous transient phenomena. NS-WD collisions may occur due to supernova kicks in a binary system or as a result of dynamic capture in a crowded environment. By leveraging AREPO, we conduct an analysis of a first-of-its-kind 3D moving-mesh magnetohydrodynamic simulation of a head on collision between a NS and WD. We demonstrate the products of this impact driven nucleosynthesis and the energy distribution of the resultant transient event. We characterize the disruption of the WD and compute the bound and unbound mass post-collision. We present this seminal work on constraining the nucleosynthetic products of this event, highlight an unusually high ^{56}Ni yield, and lay the foundations for observational follow through. We also provide discussion on avenues of further work for constraining the formation scenarios and observation of these exotic transient events.

Keywords: magnetohydrodynamics, NS-WD collision, transients

1. INTRODUCTION

The study of high energy optical and multimessenger transient phenomena, e.g. supernova (SN), has been documented in centuries of observational records (F. R. Stephenson 2017; D. W. Pankenier 2006), but has largely only been the effort of the last century of rigorous theoretical work (W. Baade & F. Zwicky 1934; J. Morán-Fraile 2024c; P. Vynatheya et al. 2025). For most of human history, optically observed transient events have been exceedingly rare. Since the advent of modern telescopes and surveys, the number of observed transients has increased by orders of magnitude (S. Gomez 2021). For example, the Pan-STARRS Survey for Transients (PSST) discovered about a thousand transients every year (M. E. Huber et al. 2020) and the Zwicky Transient Facility (ZTF) discovers tens of thousands of transients per year (E. C. Bellm et al. 2019). The start of next generation of surveys, such as the Rubin Observatory's (Rubin's) Legacy Survey of Space Time (LSST), is expected to significantly increase this rate. Rubin is expected to average at least ∼3 thousand novel SN and Luminous Transient observations per night, amounting to 10 million SN over the course of the ten year survey (M. L. Graham et al. 2024). The current epoch of multimessenger and time domain astronomy makes this boutique and detailed study of an exotic transient events all the more prescient.

A large fraction of these high energy optical transient events, particularly Supernovae (SNe), are driven by merging, colliding, and/or collapsing stars, e.g. core collapse supernova (CCSN — SN Type II, SN Type Ib, SN Type Ic (SNII, SNIb, SNIc))(F. R. Stephenson 2017; J. José 2024; A. J. Ruiter & I. R. Seitenzahl 2025). It is particularly interesting to consider the effects of catastrophic (C) close stellar interactions (CSI), which we define as interactions between two stars that disrupts or destroys one or both objects, such as mergers and collisions. For the purposes of this work we define a merger as a (C)CSI where the two objects inspiral towards each other in decaying orbits before coalescing, and a collision as a CCSI where the objects come into contact without inspiraling or mass transfer prior to impact. While there has been work on WD-

WD CCSI (J. Morán-Fraile et al. 2024a,b), NS-NS CCSI (A. Neuweiler et al. 2025; R. Ciolfi et al. 2017), Main Sequence-NS collisions CCSI (L. E. Williams et al. 2025), and even some work on WD-NS star mergers (J. Morán-Fraile 2024c; J.-P. Chen et al. 2025), NS-WD collisions in particular remain poorly constrained as do the chemical products and resultant transient events of NS collisions with non-NS objects. A WD-NS CCSI may occur from various formation scenarios:

1. A Binary or multi star system where one star evolves to a NS. The system is not disrupted by the SN of the NS progenitor, and is Darwin unstable, leading to a merger.

2. Supernova kick (SNK) where the:

   (a) NS and WD are dynamically captured resulting in a (C)CSI

   (b) NS-progentior SNK drives it into a companion WD resulting in a (C)CSI

3. Dynamical interaction in crowded clusters, e.g. W. Benz & J. G. Hills (1992)

There is ample motivation to search for WD-NS CCSIs and study their aftermaths. Stars drive much of the chemical evolution of the present epoch universe, and understanding the role that more exotic stellar interactions, such as NS-WD CCSI, play in nucleosynthesis is important to understanding everything from the formation history of galaxies (D. H. Weinberg et al. 2019; E. Toguchi-Tani et al. 2024) to the ingredients of life as we know it (T. M. Hoehler et al. 2018).

The physics of compact object CCSI are inherently extreme and therefore interesting. While compact object interactions have been studied both theoretically (P. Tang et al. 2024) and observationally (K. Kremer 2026), WD-NS collisions have not and have no well placed observational constraints. AREPO is ideal for our application due to its flexibility and scalability, because it combines advantages from both grid based models and smoothed-particle hydrodynamics models. AREPO robustly implements all the necessary physics required for our analysis and application, allowing for a boutique and detailed study of the collision. In this project, we analyse data from one of the very first expensive simulations of the head-on collision between a NS and a WD, performed with the code AREPO. We analyse the parameters of the collision, the nuclear isotopes that are generated as a result, and the energy released. We detail the chemical products of the impact driven nucleosynthesis, and discuss avenues of future work in modelling their formation and observability.

2. METHODS

This work exploits the AREPO software to run 3D magnetohydrodynamical (MHD) simulations of a NS-WD head on collision, then it analyses the outputs.

2.1. *AREPO*

AREPO makes use of a moving Voronoi mesh to simulate the evolution of a fluid, given a set of initial conditions. The points in the mesh all move with the local velocity of the fluid flow. AREPO utilises both the Lagrangian and Eulerian description of the involved matter, although it does not manages to perfectly conserve angular momentum and errors can quickly compound in complex simulations. Yet, it is still offers formidable resolution to simulations. For each time step, AREPO solves the equations of magnetohydrodynamics in each point of the mesh. At key time intervals, we take comprehensive snapshots in hdf5 file format and log changes in the state and composition of the system in a summary table. These file contains information such as density, temperature, pressure, etc for the simulation. (J. Morán-Fraile 2024c). An exhaustive validation of AREPO was not within the scope of our work, but more in depth explanation of the tool can be found in V. Springel (2010).

2.2. *Initial Conditions*

For every simulation, AREPO takes an hdf5 file with the initial conditions as input. We apply the initial conditions consistent with J. Morán-Fraile et al. (2024b). Our simulation is unique in a 3D simulation of a WD ($\approx 1M_\odot$) colliding head on with a NS ($\approx 1.4M_\odot$) rather than a merger. The initial relative velocity of the stars is chosen to be 1000 km/s at an initial separation of $4.49 \cdot 10^9$ cm. This relative velocity serves as a nominal relative velocity that can result from a SNK of the NS progenitor (S. Popov et al. 2025; T. Wagg et al.

2025b). The WD is specifically initialized as a carbon-oxygen WD $\sim (50/50)$, with trace amounts of ^{20}Ne (as can be confirmed from Figure 5). The WD is modelled to be approximately earth-size, with a central density is about $3.4 \cdot 10^7 g/cm^3$, which is a standard size for WDs of this mass. These conditions are in good agreement with O. R. Pols (2011). The NS is modelled as a point mass, this is justifiable due to numerical constraints, since it is taken to be much smaller ($R \approx 10$km) than the WD for this simulation $\sim (1/600)$. In modelling the NS as a point mass, a problem arises with the gradient of the gravitational potential, which tends to diverge as the distance between a particle and the NS becomes very small ($r \approx 0$). This would lead to a gravitational force of infinite strength, which becomes obvious from the gravitational potential:

$$\phi(r) = G\frac{m_1 m_2}{r} \qquad (1)$$

To counteract this problem, AREPO makes use of the so called gravitational 'softening length', which we set to $\approx 8 \cdot 10^7$ cm, that serves to soften/flatten the gradient of the potential very near to the NS. This allows for the simulation to be lower in resolution, and thus to model the NS as a point-mass. Should this length not be there, the potential will diverge to infinity, as will the gravitational force. The only way to solve this would be to add in an infinite amount of resolution to fully model the NS, which is computationally impossible. Detailed descriptions on how AREPO applies the softening length to the gravitational potential can be found in V. Springel (2010).

2.3. Analysis of Physical Evolution

Multiple physical parameters were analysed through time-domain analysis methods. We created and inspected several exploratory time domain plots of various physical parameters. This enabled us to get an idea of the physical evolution of the system, and determine the time of collision. We evaluated the positions for the centre of mass for the WD and NS and compared these to the centre of masses that were in the AREPO output files as a check of robustness. This was computed using the following equation for centre of mass:

$$R_{cm} = \sum_{i=1}^{N} \frac{m_i r_i}{M} \qquad (2)$$

Where m_i is the WD mass per point in the mesh, r_i is the position of the point with respect to the origin of the simulation and M is the total mass of the WD.The trajectories for the centre of masses provided help in understanding where the leftover WD matter is located post-collision. Furthermore, their separation was individually plotted with respect to time. The minimal separation was interpreted as the point of collision. The full set of snapshots was also combined to a video, with color mapped density. This video was subjected to visual inspection. The full video can be found here. A few of these snapshots are already shown in Figure 1.

Finally, to have an overview of the physical and energetic state for the leftover NS/WD bound mass post-collision, plots were made of the radial pressure, density and internal energy for the bound particles with respect to the systems centre of mass. These plots can be seen in Figure 4.

2.4. Analysis of Evolution of Ejecta

A critical step of analysis lies in quantifying the unbound mass and constraining it's evolution. To find the unbound mass, we wrote a python scrip that separates bound from unbound mass using the following bound mass criterion:

$$E_{total} = E_{kin} + E_{pot} + E_{int} < 0 \qquad (3)$$

We do not account for the NS in this calculation since it is modelled as a point mass (See 2.2. For each snapshot, a sum over the bound and unbound masses is taken. The sums get normalized to the mass of the sun and are eventually added in a plot which reveals the amount of bound and unbound mass over time. This can be seen in Figure 2.

It is important to note that the internal energy E_{int} in equation 3 is still subject of emergent discussion in the astronomical community. The difference is especially important in common envelope interactions, as illustrated in M. Vetter et al. (2025), but is negligible in the simulation considered in this work. A way to go about this is to do the calculation twice once by taking E_{int} into account and once not. Since it is more complete to consider both approaches in our work, and differences between the results of the two methods are discussed in 4.1 We created a plot (Figure 3) from the 232nd snapshot
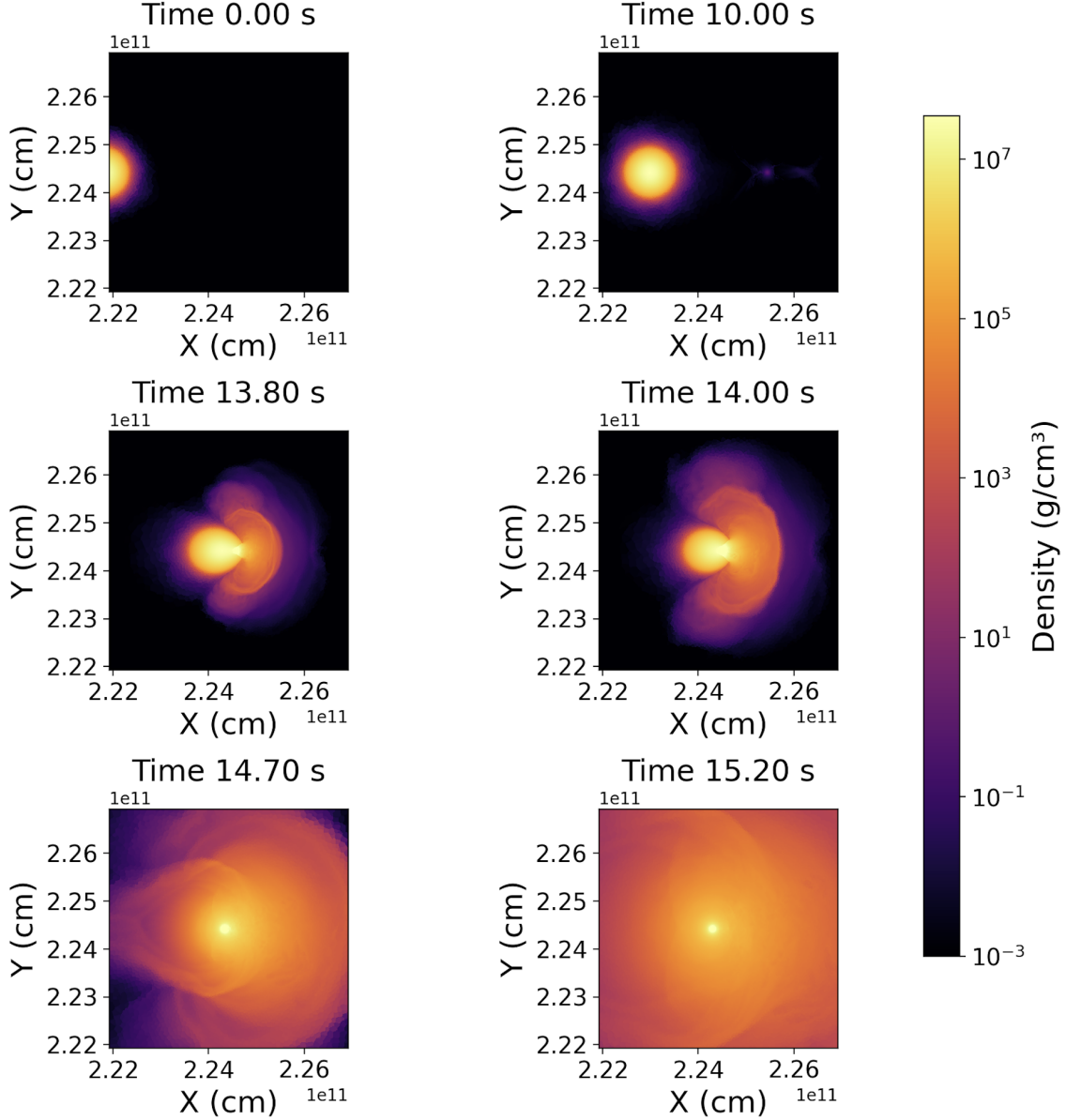
Figure 1. We demonstrate frames from our NS-WD collision The colour bar denotes the density of the gas. The NS collides the WD at t=∼14 seconds, depicted in the right panel of the second row. From left to right, top to bottom the panels depict: t= 0.00 – The objects move into the frame of view; t=10.00 – The WD and NS are visible and accelerating towards each other, t=13.8 – The WD begins to be stripped by the NS; t=14.00 – Point of minimal separation, the NS and WD have collided; t=14.70 – WD is fully disrupted, displaced material and WD 'ash' expands outwards in shell like structures; t=15.20 – The NS is at the centre of the remaining WD 'ash'. (Note that the scaling on the X and Y axis is a factor of 1e11)

that shows the magnitude of the particle radial velocity in the reference frame of the centre of mass $\|\vec{v} - \vec{v_{cm}}\|$, as a function of distance with respect to the centre of mass $\|\vec{r} - \vec{r_{cm}}\|$. This plot allows us to characterise the kinematics of the material after the collision.

2.5. Nuclear Evolution

A simplified set of 13 isotopes was coupled to the MHD simulation, in a similar way as was done by R. Pakmor et al. (2021) and S. Gronow et al. (2021). The included elements are the ones from the alpha chain: ^{4}He, ^{12}C, ^{16}O, ^{20}Ne, ^{24}Mg, ^{28}Si, ^{32}S, ^{36}Ar, ^{40}Ca, ^{44}Ti, ^{48}Cr, ^{52}Fe, and finally ^{56}Ni. The elements in
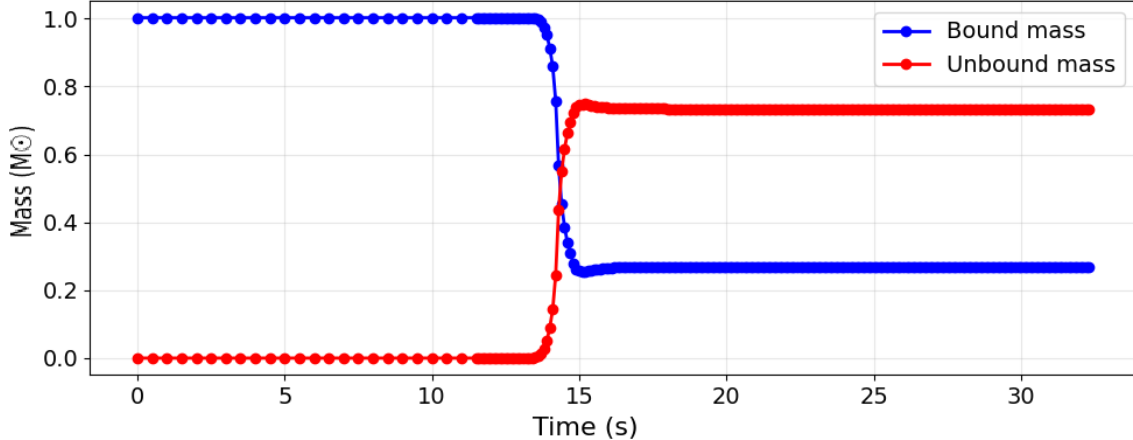
Figure 2. Plot showing the changes in the amount of bound and unbound material in a NS-WD merger through time. The mass is expressed in solar masses $M_\odot$, and does not exactly amount to one, since the mass of the WD is somewhat higher than $M_\odot$. The NS-mass is not taken into account since it is modelled as a point mass. It thus remains bound all the time anyway.

this chain are separated by capturing one or multiple ^{4}He nuclei.

To analyse the nuclear evolution, the mass fractions for each of the nuclear elements are plotted together in a stacked plot with respect to time (Figure 5). We then evaluated the total released nuclear energy with respect to time (Figure 6). This plot is made by comparing the total nuclear energy at each point to the total nuclear energy at the start. By comparing to plots from well studied transient events (e.g. CSGTs, LBOFTS, SSNIa), enabling us to evaluate similarities and/or discrepancies.

While it is possible theoretically derive the observable light curve from some of the nuclear processes, for example, the decay of ^{56}Ni, which the main driver behind supernova luminosity (J. José 2024). This is, however, well beyond the scope of our efforts and is left to future works.

3. RESULTS

3.1. *General Outcomes*

As mentioned in section 2.3, we plotted the evolution of the spatial density distribution of the WD through time in figure 1. This density plot provides intuition and context about the processes occurring through the simulation. According to the plot, the initial central density for the WD is an order of magnitude 10^7 g/cm^3, which matches the expectations given the initial conditions in section 2.2. As the WD and the NS move closer to each other, they collide at $t = 14.03$ s (see the third plot of Figure 1). After the collision, the WD

is completely disrupted: its mass is ejected and spread out from the collision point, as shown in the last three plots from the same figure, where the dense NS core is replaced by a much more diffuse structure. In the following section, we will analyse several physical parameters of significant interest from this simulation. Subsequently, the nuclear reactions induced by the collisions and synthesized isotopes will be discussed.

3.2. *Physical Results*

We first consider the plots of figure 2. These plots show what happens to the mass of the system before, during, and after the collision. As discussed earlier, a big portion of the WD's mass is ejected right after the collision. To make this quantitative, we used the criterion of bound mass ($E_{\text{tot}} < 0$), as described in Section 2.4, to separate the mass that stays bound from the mass that becomes unbound.

Before the collision, the bound mass remains steady at its maximum value. But around the time of the collision, there is a sharp drop in the amount of bound mass and a corresponding rise in unbound mass, this transition happens over about one second. In the end, the system stabilizes with $0.81 M_\odot$ bound material and about $0.19~M_\odot$ of unbound mass.

As mentioned in the section 2.4, we performed this same computation using an alternative bound mass criterion that excludes the internal energy. The percentages of the simulation´s final bounded and unbounded mass for both criteria are shown in the following table:
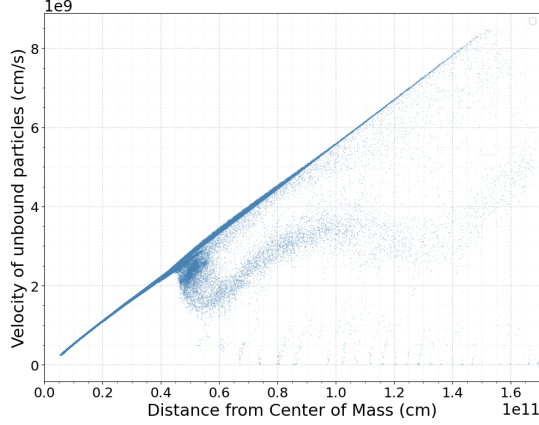
Figure 3. Velocity relative to centre of mass velocity vs radial distance from centre of mass for unbound particles at $t = 32.40s$

Table 1. Bound and unbound mass percentages for the final snapshot, with and without including internal energy

	Bound mass	Unbound mass
E_{int}	18.50 %	81.50 %
No E_{int}	18.32 %	81.68 %

It is also of great interest to discuss the velocity distribution as a function of the radial separation of the unbound particles after the collision. This distribution is shown in figure 3.

Looking at this plot, a clear linear relationship between the unbound velocity relative to the systems' centre of mass and the radial distance from the centre of mass can be seen.

Across the figure, the unbound velocities span from about 0 to 9×10^9 cm/s, while the radial distances range from approximately 0 to 1.6×10^{11} cm.

Another point to consider is that there are scattered points at larger distances but with velocities below the trend seen in the linear region. These correspond to bits of the white dwarf's atmosphere that were detached before the main collision happened.

We also found it of great interest to discuss the radial profiles of the density, pressure and internal energy of the system after the collision. (see figure 4).

The radial density profile displayed in the middle panel decreases almost linearly across the entire range, but it also features a distinct bump that shifts outward as time progresses. This bump appears around a radial distance
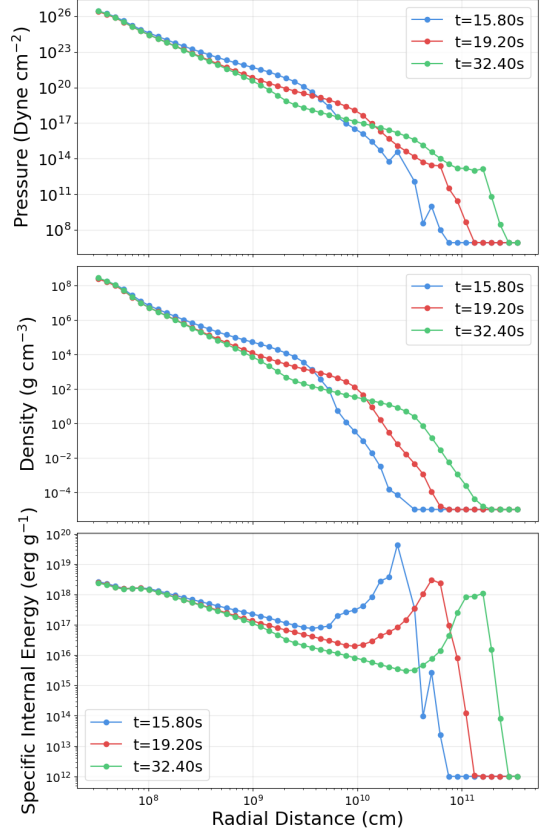
Figure 4. Radial profiles of pressure, density and specific energy of White Dwarf relative to its centre of mass

of $10^{9.5}$ cm at $t = 15.8$ s. As time passes, the bump moves outwards reaching $10^{9.9}$ cm at $t = 19.2$ s and $10^{10.4}$ cm near the end of the simulation, $t = 32.4$ s.

The pressure profile takes a similar form to the density profile: it generally decreases linearly with radius but also exhibits bumps moving outward over time. Additionally, the location of the pressure bumps coincides with the density bumps, which is an expected result, since higher density generally leads to higher pressure.

In the bottom panel, the specific internal energy also shows a decreasing trend with radius, but features a sharper peak that exceeds the value of the internal energy closer to the centre of mass. After the collision, this peak is positioned near $10^{10.3}$ cm, then migrates to $10^{10.8}$ cm, and finally to $10^{11.2}$ cm as time progresses. This moving peak highlights regions where collision-driven heating is most intense, and its outward migration tracks the expansion and cooling of ejected material.

3.3. *Nuclear Evolution*

In figure 5 we plotted the temporal evolution of mass fractions for the 13 resulting isotopes, introduced in Section 2.5. At the beginning of the simulation, the WD is composed of roughly 50% of ^{16}O and 50% of ^{12}C with minor traces of ^{20}Ne. After the collision, a spike in ^{4}He production is observed. Following this, heavier elements are also synthesized, which reduces the initially generated amount of ^{4}He. These nuclear processes occur rapidly, within less than one second. From that moment on, the mass fraction of each of the isotopes stabilize. Looking at the outcome of the collision after the stabilization, the most noticeable result is the great amount of ^{56}Ni that is produced, which constitutes 76% of the total resulting isotopic mass. Despite the decrease of ^{4}He, it is still the second most abundant isotope once stability is achieved, with 11% of the total mass. It is worth noting that the remaining amounts of ^{12}C and ^{16}O isotopes from the beginning of the simulation become negligible after the collision. As a result of nuclear isotopic synthesis, it is expected that nuclear energy would also be released from the system. Following the method discussed in section 2.5, we plotted the released nuclear energy due to the isotopic production in figure 6. Before the collision, as expected, there is no nuclear energy being released. Once the collision occurs, a small dip in the nuclear energy is observed reaching a minima of -0.3×10^{51} erg, which coincides in time with the initial production of ^{4}He discussed previously. Immediately following that, and in synchronization with the production of the heavier isotopes, a significant amount of energy is released, reaching an energy of 1.2×10^{51} erg.

4. DISCUSSION

The use of MHD simulations can provide detailed and boutique insights into interactions that are difficult to constrain observationally. Using AREPO, we were able to simulate a head on collision of a WD and NS and to place key constraints on the physical parameters and chemical products of the collision, especially the ^{56}Ni ejection mass

4.1. *Discussion of Key Results*

Reviewing the output obtained in section 3.2, we concluded that 81% percent of the total WD's mass becomes unbound, while 19% percent remains bounded after the collision. This means that most of the WD's mass is ejected and escapes the system in the NS-WD collision.

Hints of this phenomenon can also be seen in the middle panel of figure 4: the discussed density peak moves outward from the systems centre of mass over time, which reflects the ejection of WD material following the collision.

Over long timescales, we would expect the discussed bound material to remain near the neutron star, forming a cloud centred around it. However, in this simulation, the observed period is not long enough for the collapse to manifest, as such, these results should serve as a basis for future investigation rather than definitive conclusions.

We also address how the selected criteria for defining bound and unbound matter, as presented in Section 3, influence the resulting mass fraction estimates. As we can observe in table 1, the difference in bound and unbound mass fraction due to the different criteria is minimal, with a difference in percentage of $\sim 0.18\%$. Therefore, for all remaining results, we used equation 3 as the energy criteria to classify bound and unbound masses with no additional distinction. However, it is still of great interest to mention that in some astropysical scenarios, which fall beyond the scope of this project, such as in common-envelope interactions (M. Vetter et al. (2025)), this difference in criteria can not be ignored.

Another notable aspect examined is the linear correlation observed between the unbound velocity and radial distance. This can be observed in figure 3.2. This proportionality is known as homologous expansion, a phenomenon frequently observed in astrophysical explosions (ciation needed) where material moves outward such that its velocity linearly increases as a function of distance. Finally, a quantitative analysis of isotopic production and the order of magnitude of nuclear energy release is presented. As mentioned in section 3.3, immediately following the collision, a significant amount of ^{4}He is produced within a brief period, coinciding with a minimum in the nuclear energy released (figure 6. This behaviour is due to the high temperatures achieved at the moment of impact, which promotes photodisintegration processes S. E. Woosley & W. M. Howard (1978). Under this conditions, the initial abundances of ^{12}C and
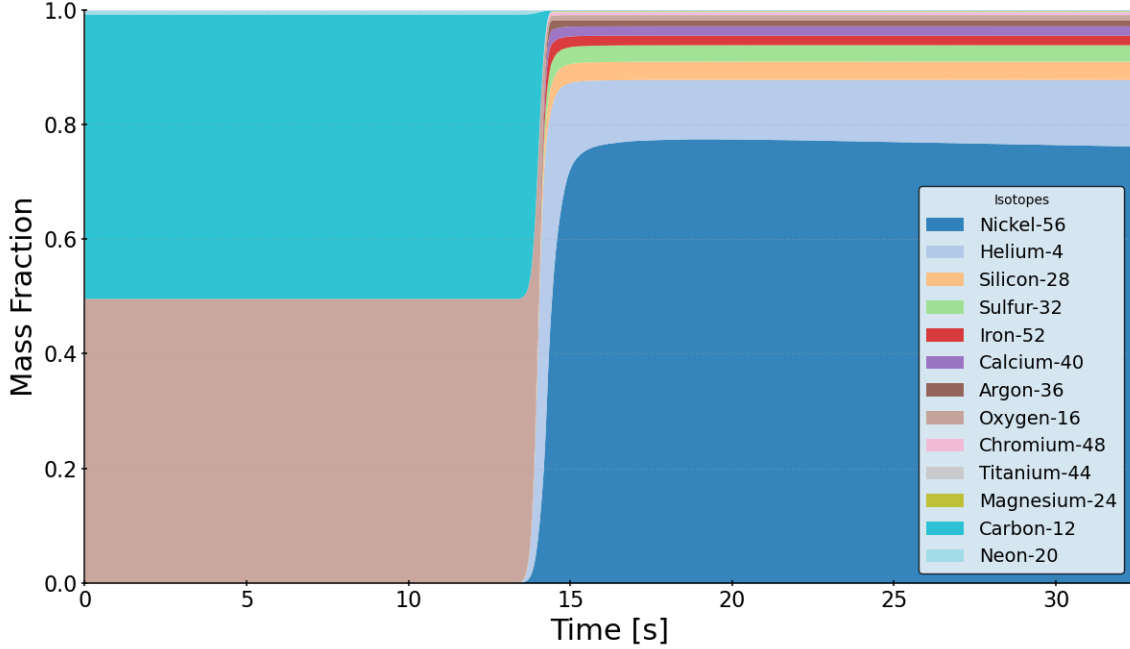
Figure 5. The evolution of isotopic mass fractions through time as the WD-NS merger takes place. Until about t = 13.5s, it clearly shows the oxygen-carbon composition of the WD, with a trace amount of neon-20 (not visible in the plot). After full disruption of the WD at about t = 15s, a fraction of nearly 0.8 of the mass is accounted for by nickel-56, the main driver of luminosity in this event J. José (2024). It also follows from the plot that an amount helium-4 is produced. This makes up for about 0.1 of the total fraction. Some other elements (all included in the alpha chain mentioned in 2.5) make up the remaining amount of the fraction.
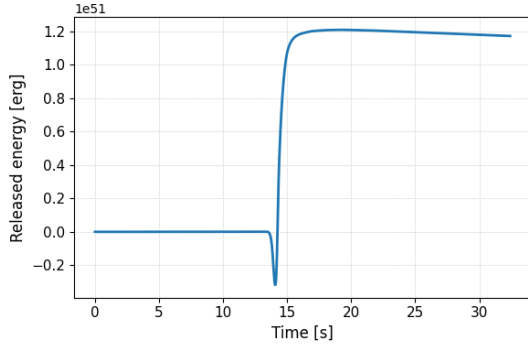
Figure 6. Released nuclear energy over time for our NS-WD collision. Until the point of collision at t=∼14.00, there is no release or loss of nuclear energy. At the time of collision and right after it, the figure shows a drop in nuclear energy, which is due to the photo disintegration of elements into ^{4}He. After the disintegration, when enough helium has been created, a spike in the released nuclear energy is seen at t=15.00, which is due to the radiative decay of ^{56}Ni by gamma decay.

^{16}O undergo nuclear reactions resulting in the production of ^{4}He. Because the binding energy per nucleon for ^{4}He is lower than that for ^{16}O and ^{12}C, the net nuclear energy re-

leased exhibits a temporary reduction. While ^{4}He is being produced, we previously mentioned that heavier elements are also produced in the meantime. This is due to the nuclear alpha capture chain. This phenomena also explains the decrease in the abundance of ^{4}He. Additionally, the synthesis of heavier nuclei, such as ^{56}Ni, which have higher binding energies per nucleon, corresponds to an increase in the nuclear energy released in subsequent phases. We would like to emphasize two key results from this discussion: ^{56}Ni emerges as the most abundant synthesized isotope in our simulation, which is of significant interest due to its brief half-life and decay by gamma emission, contributing substantially to the luminosity produced. Additionally, the peak value for released nuclear energy reaches an order of magnitude of approximately $\sim 10^{51}$,consistent with the typical energies inferred for super luminous supernovae, as reported in P. Schneider (2015).

4.2. Future Work

In order to demonstrate the robustness of our results we would need to analysis variations

of this original simulations in order to separate which results are intrinsic to NS-WD collisions versus this NS-WD Collision. We would need to consider alternate collisions such as an off-centre impact and grazing-encounter. By studying an ensemble of simulations we can place better constraints on the exact nature of these CCSI. While we can point to multiple possible formation scenarios for NS-WD CCSI, and the effort constraining the nature and abundance of these scenarios presents a fertile avenue for further work. In particular investigating what binaries evolution scenarios may result in NS-WD coalescence, determining which ones are the most robust. Tools such as Compass (J. Riley et al. 2022), Cogsworth (T. Wagg et al. 2025a), and Legwork (T. Wagg et al. 2022) can allow zoomed out explorations of these formation scenarios. Using Legwork it might be possible to constrain gravitational wave signals, as ones that might be detectable by LISA mission (M. Colpi et al. 2024). Converting the energy profiles to a optical light curve, spectroscopically measurable chemical abundances, spectral energy distribution or other key observables presents is a non trivial endeavour. However, with significant future effort work it is possible model these. By analysing the structure of the released energy curve, we can link this to specific nuclear processes. In particular, a process like photodissociation of elements into ^{4}He, or the radiative decay of ^{56}Ni by gamma radiation O. R. Pols (2011).

4.2.1. *Characterising the Remnant*

Finaly it is note worthy that there is a remnant that survives this NS-WD CCSI, as can be seen in the bottom right panel of Figure 1

4.3. *Final Takeaway/impact*

Understanding the deaths of stars and their aftermaths not only helps us place key constraints on stellar evolution and allow for interesting exploration of transient events, but contextualise their broader impact on larger areas of astronomy such as the composition of the interstellar medium (ISM), galactic evolution, and origins of life. The present epoch of astronomy simultaneously presents an incredible capacity for both detailed theoretical simulations and a tremendous volume of observational data E. Bellm et al. (2019). Modern MHD stimulations like AREPO allow us to make detail exotic astrophysical events and the next-generation telescopes like Vera Rubin and its Legacy Survey of Space and Time will provide and opportunity to find them. By providing the key constraints on the physics of a NS-WD collisions we have not only lay the foundation for understanding the high energy astrophysics at play, but present an opportunity to bridge the theoretical models of exotic close stellar interactions and to apply them to the study of the once rare high energy transient events.

5. APPENDIX

REFERENCES

Astropy Collaboration, Price-Whelan, A. M., Lim, P. L., et al. 2022, ApJ, 935, 167, doi: 10.3847/1538-4357/ac7c74

Baade, W., & Zwicky, F. 1934, Proceedings of the National Academy of Science, 20, 254, doi: 10.1073/pnas.20.5.254

Bellm, E., Ford, E. B., Tohuvavohu, A., et al. 2019, in Bulletin of the American Astronomical Society, Vol. 51, 125, doi: 10.48550/arXiv.1907.07817

Bellm, E. C., Kulkarni, S. R., Graham, M. J., et al. 2019, PASP, 131, 018002, doi: 10.1088/1538-3873/aaecbe

Benz, W., & Hills, J. G. 1992, ApJ, 389, 546, doi: 10.1086/171230

Chen, J.-P., Shen, R.-F., & Chen, J.-H. 2025, arXiv e-prints, arXiv:2510.27399, doi: 10.48550/arXiv.2510.27399

Ciolfi, R., Kastaun, W., Giacomazzo, B., et al. 2017, PhRvD, 95, 063016, doi: 10.1103/PhysRevD.95.063016

Colpi, M., Danzmann, K., Hewitson, M., et al. 2024, arXiv e-prints, arXiv:2402.07571, doi: 10.48550/arXiv.2402.07571

Gomez, S. 2021, PhD thesis, Harvard University, Massachusetts

Graham, M. L., Bellm, E. C., Guy, L. P., et al. 2024, DMTN-102: LSST Alerts: Key Numbers,, Rubin Observatory Technical Report, 2024 doi: 10.71929/RUBIN/2997858

Gronow, S., Collins, C. E., Sim, S. A., & Röpke, F. K. 2021, A&A, 649, A155, doi: 10.1051/0004-6361/202039954

Hoehler, T. M., Som, S. M., & Kiang, N. Y. 2018, in Handbook of Exoplanets, ed. H. J. Deeg & J. A. Belmonte, 74, doi: 10.1007/978-3-319-55333-7_74

Huber, M. E., Chambers, K., Smartt, S. J., Smith, K. W., & Pan-Starrs Transient Team. 2020, in American Astronomical Society Meeting Abstracts, Vol. 235, American Astronomical Society Meeting Abstracts #235, 306.04

Hunter, J. D. 2007, Matplotlib: A 2D graphics environment, IEEE COMPUTER SOC, doi: 10.1109/MCSE.2007.55

José, J. 2024, in European Physical Journal Web of Conferences, Vol. 297, European Physical Journal Web of Conferences (EDP), 01006, doi: 10.1051/epjconf/202429701006

Kremer, K. 2026, in Encyclopedia of Astrophysics, Volume 3, Vol. 3, 458–472, doi: 10.1016/B978-0-443-21439-4.00103-6

Morán-Fraile, J. 2024c, PhD thesis, U. Heidelberg (main), doi: 10.11588/heidok.00034803

Morán-Fraile, J., Holas, A., Röpke, F. K., Pakmor, R., & Schneider, F. R. N. 2024a, A&A, 683, A44, doi: 10.1051/0004-6361/202347769

Morán-Fraile, J., Röpke, F. K., Pakmor, R., et al. 2024b, A&A, 681, A41, doi: 10.1051/0004-6361/202347555

Neuweiler, A., Dietrich, T., & Brügmann, B. 2025, Phys. Rev. D, 112, 023033, doi: 10.1103/tsg2-bp7l

OpenAI. 2025, Introducing GPT-5,, https://openai.com/index/introducing-gpt-5/

Pakmor, R., Zenati, Y., Perets, H. B., & Toonen, S. 2021, Monthly Notices of the Royal Astronomical Society, 503, 4734–4747, doi: 10.1093/mnras/stab686

pandas development team, T. 2020, pandas-dev/pandas: Pandas, latest Zenodo, doi: 10.5281/zenodo.3509134

Pankenier, D. W. 2006, Journal of Astronomical History and Heritage, 9, 77

Pols, O. R. 2011, Stellar Structure And Evolution (Astronomical Institute Utrecht). https://www.ucolick.org/~woosley/ay112-14/texts/pols11.pdf

Popov, S., Müller, B., & Mandel, I. 2025, NewAR, 101, 101734, doi: 10.1016/j.newar.2025.101734

Riley, J., Agrawal, P., Barrett, J. W., et al. 2022, ApJS, 258, 34, doi: 10.3847/1538-4365/ac416c

Ruiter, A. J., & Seitenzahl, I. R. 2025, A&A Rv, 33, 1, doi: 10.1007/s00159-024-00158-9

Schneider, P. 2015, Extragalactic Astronomy and Cosmology: An Introduction, doi: 10.1007/978-3-642-54083-7

Springel, V. 2010, Monthly Notices of the Royal Astronomical Society, 401, 791–851, doi: 10.1111/j.1365-2966.2009.15715.x

Stephenson, F. R. 2017, in Handbook of Supernovae, ed. A. W. Alsabti & P. Murdin, 49, doi: 10.1007/978-3-319-21846-5_44

Tang, P., Eldridge, J. J., Meyer, R., et al. 2024, MNRAS, 534, 1707, doi: 10.1093/mnras/stae2154

Team, G., Anil, R., Borgeaud, S., et al. 2025, Gemini: A Family of Highly Capable Multimodal Models, https://arxiv.org/abs/2312.11805

Toguchi-Tani, E., Spoo, T., Frinchaboy, P., & Tayar, J. 2024, in American Astronomical Society Meeting Abstracts, Vol. 243, American Astronomical Society Meeting Abstracts #243, 458.03

Vetter, M., Röpke, F. K., Schneider, F. R. N., et al. 2025, A&A, 698, A133, doi: 10.1051/0004-6361/202554685

Vynatheya, P., Ryu, T., Wang, C., Sills, A., & Pakmor, R. 2025, arXiv e-prints, arXiv:2510.13736, doi: 10.48550/arXiv.2510.13736

Wagg, T., Breivik, K., & de Mink, S. E. 2022, ApJS, 260, 52, doi: 10.3847/1538-4365/ac5c52

Wagg, T., Breivik, K., Renzo, M., & Price-Whelan, A. M. 2025a, ApJS, 276, 16, doi: 10.3847/1538-4365/ad8b1f

Wagg, T., Hendriks, D. D., Renzo, M., & Breivik, K. 2025b, The Open Journal of Astrophysics, 8, 85, doi: 10.33232/001c.141718

Weinberg, D. H., Holtzman, J. A., Hasselquist, S., et al. 2019, ApJ, 874, 102, doi: 10.3847/1538-4357/ab07c7

Weinberger, R., Springel, V., & Pakmor, R. 2020, The AREPO Public Code Release, American Astronomical Society, doi: 10.3847/1538-4365/ab908c

Williams, L. E., Chang, P., Levesque, E. M., & Quinn, T. R. 2025, ApJ, 993, 61, doi: 10.3847/1538-4357/ae100d

Woosley, S. E., & Howard, W. M. 1978, ApJS, 36, 285, doi: 10.1086/190501